Materials Science and Technology 31 (2015) 1735-1744

Dry rolling/sliding wear of nanostructured pearlite

S. Das Bakshi[a], A. Leiro[b], B. Prakash[b], H. K. D. H. Bhadeshia[a]

[a] *Materials Science and Metallurgy, University of Cambridge, U.K.*

[b] *Applied Physics and Mechanical Engineering, Luleå University of Technology, Sweden*

Abstract

The dry rolling-sliding wear behaviour of pearlite that has an interlamellar spacing of just 85 nm has been characterised. Its wear resistance is found to be comparable to that of much harder bainitic steels. Microstructural observations indicate that there is substantial plastic deformation of both the ferrite and cementite components of the pearlite in the vicinity of the wear surface. The plasticity is not expected from Hertzian analysis that assumes a smooth contact surface. It is likely instead to be a consequence of exaggerated stresses due to surface roughness. The material remains ductile to shear strains of the order of 4. Diffraction data indicate that the coherent domain size is reduced to about half the interlamellar spacing and that some of the cementite may dissolve and contribute to the expansion of the lattice parameter of ferrite.

Keywords: dry rolling/sliding, nanostructured pearlite, Hertzian contact, residual stress, X-ray diffraction.

1. Introduction

The dry wear behaviour of pearlite has been characterised in the past as a function of contact load [1–5], relative slip [1, 3–8], chemical composition [3, 9–11], mechanical properties [8, 9, 12] and microstructure [3, 8, 10, 12–15]. One clear conclusion is that the rolling/sliding wear resistance of pearlite is enhanced by reducing the distance between ferrite (α) and cementite (θ) lamellae [8, 9, 12].

Refined pearlite has a greater flow stress and work-hardening rate, both of which lead to a reduction in the wear rate [12, 15, 16], although the fatigue strength is insensitive to the interlamellar spacing [17, 18]. Finer cementite is able to accommodate more deformation prior to fracture so the pearlite is able to flow in a narrow zone at the wear surface [19, 20].

The purpose of the present work was to study the rolling/sliding wear behaviour of particularly fine pearlite with interlamellar spacing of the order of 85 nm. With appropriate alloying, such pearlite can be produced by heat-treatments that do not involve rapid cooling or transformation at large undercoolings. Similar work has recently been reported on pearlite produced by isothermal transformation, but under conditions of severe slip (20%) in order to simulate extreme wear at railheads on curved tracks, whereas the present work is limited to 5% slip in order to permit comparisons against other microstructures tested under the same conditions [21].

2. Experimental Procedures

2.1. Alloy and heat treatment

Extremely fine pearlite with interlamellar spacing <50 nm has been found to form during the continuous cooling of the Fe-0.8C-1.6Si-1.9Mn-1.3Cr-0.30Mo alloy, that also has major applications in the form of a fine mixture of bainitic ferrite and retained austenite [22, 23]. The alloy was continuously cast in the form of a 150 mm diameter ingot after electroslag refining with the chemical composition listed in Table 1. Flat-faced cylindrical rings for rolling/sliding test, with outer and inner radii equal to 22.5 ± 0.1 mm and 17.5 ± 0.1 mm respectively, were cut using electro-discharge machining. The curved faces of the discs were then ground to a final roughness of $\approx 1\,\mu$m in order to ensure smooth contact during rolling/sliding. A pair of discs was then heat treated in a sealed tube furnace under containing an atmosphere of 99.5% pure argon flowing at $2\,\mathrm{l\,min^{-1}}$. Details of the heat treatment and the Vicker's hardness values based on ten different locations are in Table 1; the philosophy behind the alloying is explained in [22, 23].

Table 1: Chemical composition (wt %), heat treatment and resultant hardness measured using a 30 kg load.

C	Mn	P	S	Si	Al	Cu	Cr	Mo	V	Co	Sn	Nb
0.83	2.28	0.011	0.008	1.9	0.044	0.12	1.44	0.24	0.11	1.55	0.019	0.023

Heat Treatment	Vickers hardness
930 °C 1 h, air cooled to 550 °C, held for 4 hours, air cooled	378 ± 9

2.2. Wear tests

Rolling/sliding wear tests were performed on the heat treated discs in a servo-hydraulic UTM 2000 twin-disc machine. The discs were made to overlap at 5 mm distance over their widths, i.e., 50% of their width. A roll-slide parameter $\xi = 0.95$, was introduced by administering differential velocities (100 and 95 rpm respectively) between the discs.[1] The tests were conducted in a controlled environment at $\sim 25\,^{\circ}$C and 23% humidity, without any lubrication. Experiments were conducted for three pairs of discs for 30,000 cycles with an externally applied load equal to 300 N. Weight losses were measured for three pairs of discs and normalised against load and the distance traveled by a point on the perimeter over the duration of test. [2]

2.3. Metallography

Samples were characterised using scanning electron (Jeol 5800 LV) and transmission electron (Jeol 200 CX) microscopy. For scanning microscopy, the metallographically ground and polished samples were etched with 2 volume % nital. Thin foils for transmission microscopy were prepared by cutting $\sim$200 µm thick samples using a SiC blade, from which discs of 3 mm diameter were

[1] The parameter is calculated from the difference of circumferential velocities of the two discs. Mathematically, it is 1-(% slip/100).

[2] It is worth emphasising that the measured temperature of the sample never exceeded 29°C during the tests.

machined out using spark-erosion. The discs were then ground down to 50 μm thickness using 2500 and 4000 grit SiC abrasive papers successively and foils were prepared by electro-polishing at -4°C in an electrolyte comprising of 5% perchloric acid, 15% glycerol and 80% methanol by volume.

2.4. Nanoindentation tests

To assess the hardness on the scale of microstructural damage, constant-depth (400 nm) nanoindentation tests were performed using a pyramidal Berkovich indenter. The cross section of the rolling/sliding specimen was polished in 0.40 μm colloidal silica for 5 mins to achieve a surface roughness less than the indenter penetration-depth. The machine was calibrated using a fused silica standard. Indents were made starting at the near-surface region and progressing towards the underlying material that is unaffected by the wear test. Hardness was calculated from the slope of the unloading part of the load-displacement curve according to [24]. Residual stress in the sub-surface region was estimated as in [25–28].

2.5. X-ray diffraction

A Philip's PW1730 vertical X-ray diffractometer was used with the Bragg-Brentano geometry under a continuous scanning mode over 2θ = 38-150° with a scan step of 0.03° and dwell time of 14 s per step, using Cu_{K_α} radiation so that much of the diffracted information comes from a depth of about 1 μm. A 150 μm flat slice was cut from the curved surface using electro-discharge machining. This was polished down to 60 μm using diamond abrasives. The polished surface was then subjected to X-ray diffraction, with the experiment repeated after electropolishing so that the data could be resolved as a function of depth. The diffracted beam out of the surface was focused on a curved graphite monochromator through an anti-scatter slit of 0.2° and a receiving slit of 0.5°. Standard strain-free crystals of LaB_6 were diffracted in the same instrument over a 2θ range of 20-150° in order to measure the instrumental broadening using the Caglioti equation,

$$\beta_{\text{standard}} = \sqrt{u \tan^2 \theta + v \tan \theta + w} \tag{1}$$

The Caglioti parameters using LaB_6 spectra obtained after full profile fitting in ProFit are $u = 0.004531$, $v = 0.000513$ and $w = 0.007907$ respectively. These parameters are then used to calculate instrumental broadening as a function of θ. Conventional Williamson-Hall plots were made for the ferrite peaks after stripping off the instrumental broadening and assuming a pure Lorentzian or a Gaussian shape; a better analysis using a modified Williamson-Hall approach as described in [29, 30] was also implemented.

3. Results and Discussions

3.1. Microstructure

Fig.1a shows the completely pearlitic structure obtained, without any proeutectoid phases which are known to be detrimental to mechanical properties [31]. The true interlamellar-spacing, $\overline{L}_0$, was measured to be 85 ± 7 nm on transmission electron micrographs (Fig.1b) using Underwood's intersection method [32]. This can also be taken as the mean free path within ferrite, a parameter that influences the strength and work-hardening rate of pearlite [16]. The hardness achieved is compared against published data in Fig.1c, a plot that indicates an approximately linear relationship between hardness and the reciprocal of the interlamellar spacing [33] although it is noted that a Hall-Petch type relationship can be used with similar fit within the limits of experimental data [34, 35].

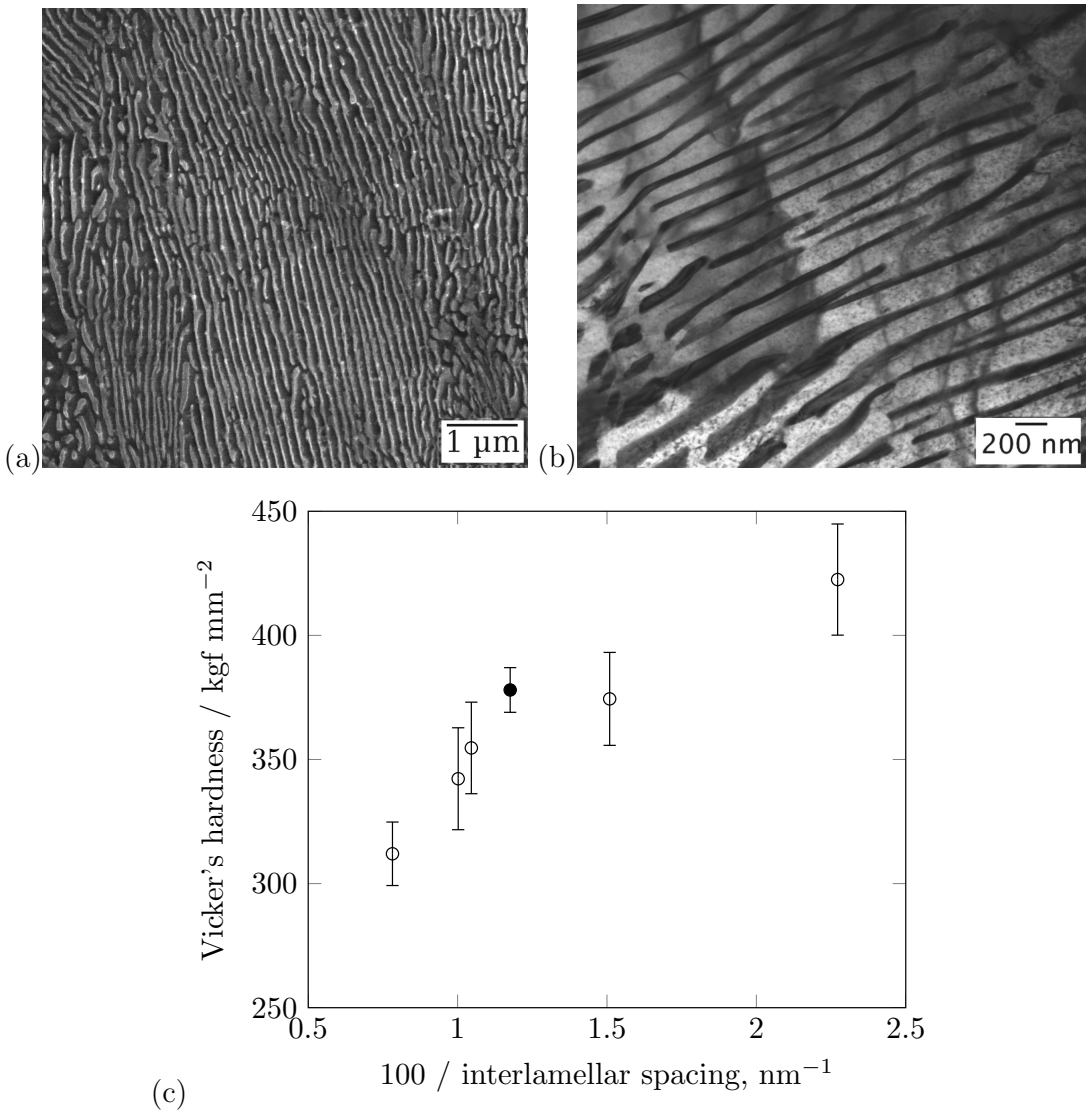

Figure 1: (a) Secondary electron image of the fine pearlite [36], (b) TEM image showing fine alternate arrangement of ferrite and cementite and (c) comparison of bulk hardness against interlamellar spacing of experimental alloy (closed circle) and other nanostructured pearlite (open circles) [22].

3.2. Wear observations

As expected, surface roughness increased following rolling/sliding, but a comparison with much harder nanostructured bainite (Table 2) tested under the same circumstances shows that the extent of roughening is greater by a factor of about 3 in the average roughness following testing. It is known that contact pressures become greater with rough surfaces when compared against those that remain smooth, resulting in sub-surface plastic deformation extending to tens of micrometres even though the nominal loading should leave the material in an elastic state [37].

Table 2: Surface roughness parameters of discs before and after rolling/sliding. Data for nanostructured bainite [38] are presented for comparison.

	Disc 1		Disc 2	
	before test	after test	before test	after test
Nanostructured pearlite, 378 kgf-mm^{-2}				
Average roughness R_a/ µm	1.2	3.0	1.2	2.6
Distance between highest crest and lowest trough R_z/ µm	1.5	3.8	1.4	3.4
Maximum height of ridges R_t/ µm	8.1	29.2	8.2	25.2
Nanostructured bainite, 640 kgf-mm^{-2}, [38]				
R_a/ µm	1.3	1.1	1.1	1.1
R_z/ µm	7.0	13.9	7.0	11.4
R_t/ µm	7.5	15.2	7.2	11.8

In spite of the development of roughness, Fig. 2 shows good specific-wear resistance for the nanostructured pearlite, both when compared against somewhat softer pearlitic steels, and against a variety of bainitic steels, some of which are much harder (even harder bainitic steels do of course show a smaller wear rate). These comparisons are made for steels studied under identical conditions to the present work [39]. The work emphasises the fact that techniques of estimating wear simply on the basis of phase fractions [40] or hardness are unlikely to correctly predict wear resistance, when mechanisms of wear are dependent on the details of the structure.

3.3. Dynamic coefficient of friction

The stresses experienced by the steel have been calculated for rolling-sliding contact as described elsewhere in detail [38], based on Hertzian contact theory [41, 42]. The computer programs for doing such calculations have been made available freely on:

http://www.msm.cam.ac.uk/map/steel/programs/contact.html

Based on the observed range of dynamic friction coefficients (Fig.3) calculations indicate that the corresponding variations in the stresses experienced are negligible, fluctuation is most prominent in tractional stress, σ_x =379-385 MPa, $-\sigma_z = 441.7 \pm 0.2$ MPa and maximum shear stress, $-\tau_{xz}$ = 115-113 MPa.

Fig. 4 shows how the stresses are distributed on the xz plane. Given that the simulation is for a small amount of slip (5%), it is expected that the maximum shear stress occurs below the contact surface, at a depth of about 50 µm. However, the analysis is not properly representative, for example, the shear stress calculated at the surface is quite small < 100 MPa), which is surprising because there is clear evidence of plastic deformation to a depth of at least 40 µm. This can be seen in the scanning electron micrographs presented in Fig. 5. The explanation must lie in the fact that the calculations assume a smooth surface, whereas it is far from smooth once

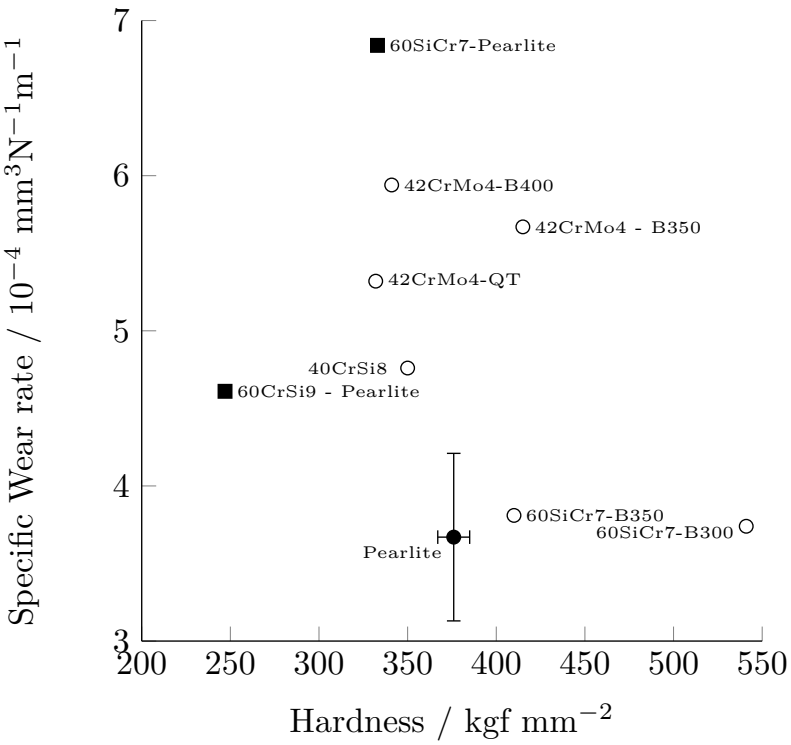

Figure 2: Specific wear rates measured in rolling/sliding tests. The open circles represent bainitic steels [39], and the filled points pearlite (square from [39] and circle: present work).

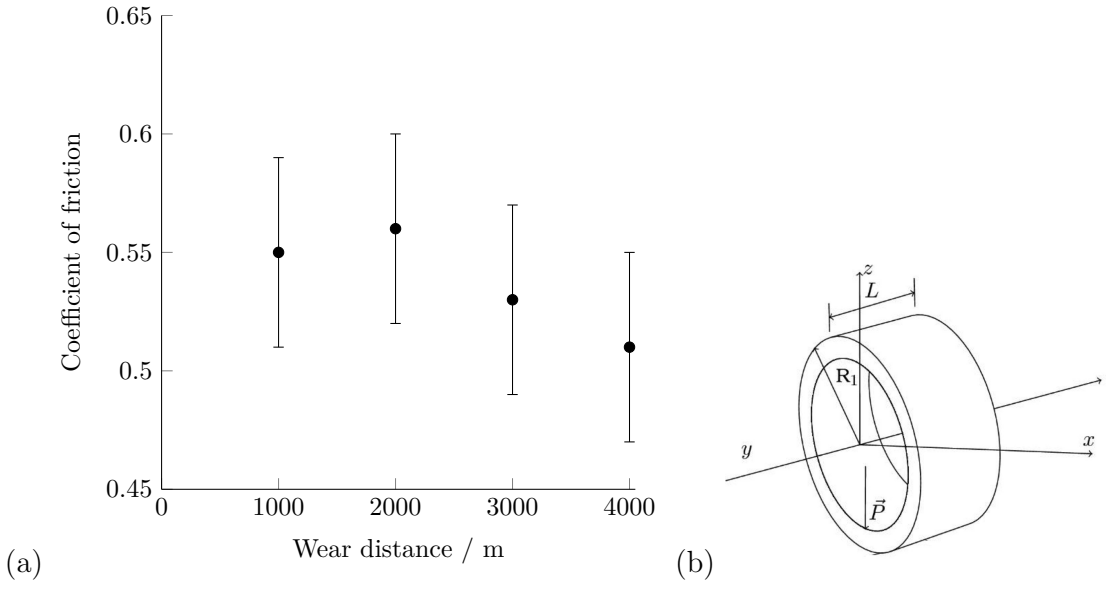

Figure 3: (a) Measured dynamic coefficient of friction as a function of the wear distance, (b) Coordinate system.

the wear process begins (Table 2). As already noted in section 3.2, the consequence of roughness is to exaggerate stresses and induce plastic deformation. Therefore, the calculated shear stress is the minimum stress that could be experienced with a geometrically smooth surface, whereas the actual stress are undoubtedly greater. Similar experience has been found in rails, where the operating contact pressure is kept below the shakedown limit of pearlitic rail steel [43], but there is nevertheless severe plastic deformation observed to a depth of tens of micrometres because of the higher stresses experienced at asperities associated with surface roughness [37]. Surface roughness that persists during the wear test causes the contact pressures to far exceed those associated with the smooth surface theory.

Fig. 5 also shows that there is significant plasticity even in the cementite that is deformed in the vicinity of the contact surface. Although frequently regarded as a brittle phase, it is well-known to behave in a ductile manner when the cementite lamellae are fine [44, 45] and such plasticity is a common feature of the surfaces of worn rail steels [21, 37]. It is noteable that although the surface roughness is in the range $R_a = 14 - 3\,\mu$m (Table 2), the depth of plastic deformation extends down to some 40-50 µm. It is likely that the primarly effect of the roughness is to cause through friction, the shearing of a deeper region of the material which is not intrinsically hard.

3.4. Nanoindentation results

The hardness derived from the nano indentation load-displacement curves [24] is shown in Fig. 6(a) as a function of the depth below the contact surface. An increase of about 1 GPa occurs relative to the bulk, which is consistent with the X-ray derived structural information reported below, and recent observations on pearlite wear in a Fe-1C-0.7Mn-0.4Si-0.25Cr steel [21]. The observed surface hardening below the surface is considered beneficial towards reducing wear in pearlite as long as it does not lead to excessive detachment of wear particles [4, 46–48].

Fig. 6(b) shows the elastic recovery following removal of the indentation load, a phenomenon indicative of the presence of residual stresses, which can be estimated by studying the indent residual-depth and residual cone-angle after removal of the applied load [25–28]. Fig.6(c) shows that the stress in the plane parallel to the wear surface is compressive in the direction of rolling sliding; it is this which is known to control wear [49, 50]. It should be emphasised that the stresses measured cover approximately five grains and hence refer to type II residual stress [51], but the compressive nature should nevertheless help in resisting the applied traction stress σ_x.

3.5. X-ray diffraction

The observed X-ray peak broadening is indicative of the state of the microstructure following abrasion (Fig. 7), and can be used to estimate the size of the coherent domains along with the residual microstrain within the crystallites. These two parameters can be deconvoluted by plotting the peak width at half the maximum height (FWHM in radians) $\mathrm{K} = 2\sin\theta/\lambda$ where θ is the Bragg angle and λ is the X-ray wavelength. This is known as the Williamson-Hall plot, but as seen in Fig. 8(c-d), revealed rather poor correlation to the plotting function.

As a consequence, elastic anisotropy was taken into account in the analysis [52–54], replacing the function $K = 2\sin\theta/\lambda$ by $K\sqrt{\bar{C}}$, where $\bar{C}$ is the average dislocation contrast factor for a specific *hkl* plane. The diffraction profiles of {110},{002}, {112}, {022}, {013} and {222} have been considered for the analysis. The modified Williamson-Hall model used for calculation is

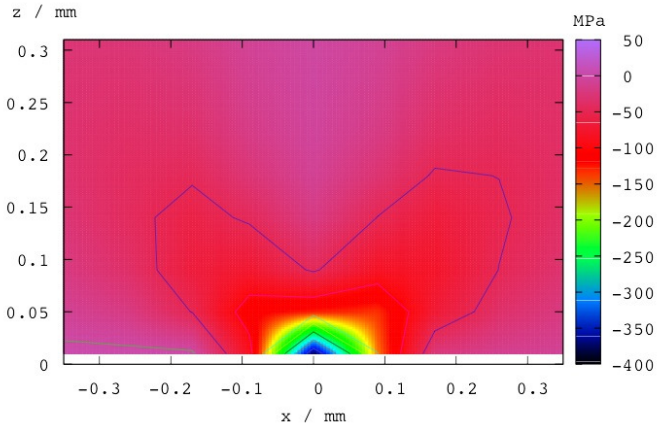

(a) σ_x

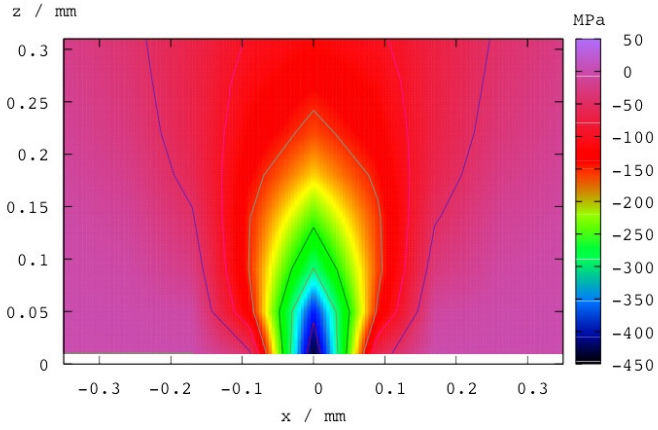

(b) σ_z

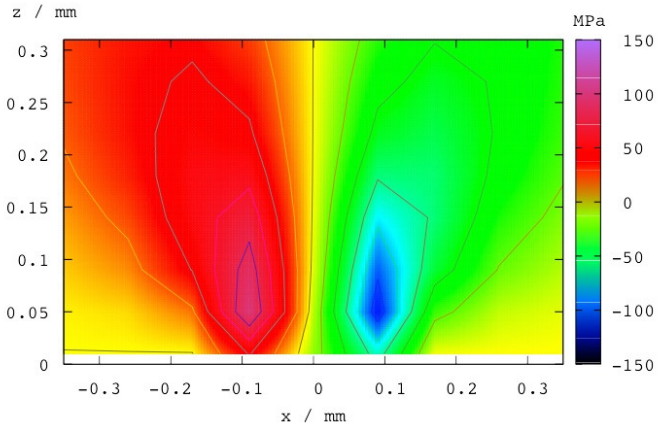

(c) τ_{xz}

Figure 4: Stress distributions calculated assuming $\mu = 0.57$ and $d = 4000\,\mathrm{m}$.

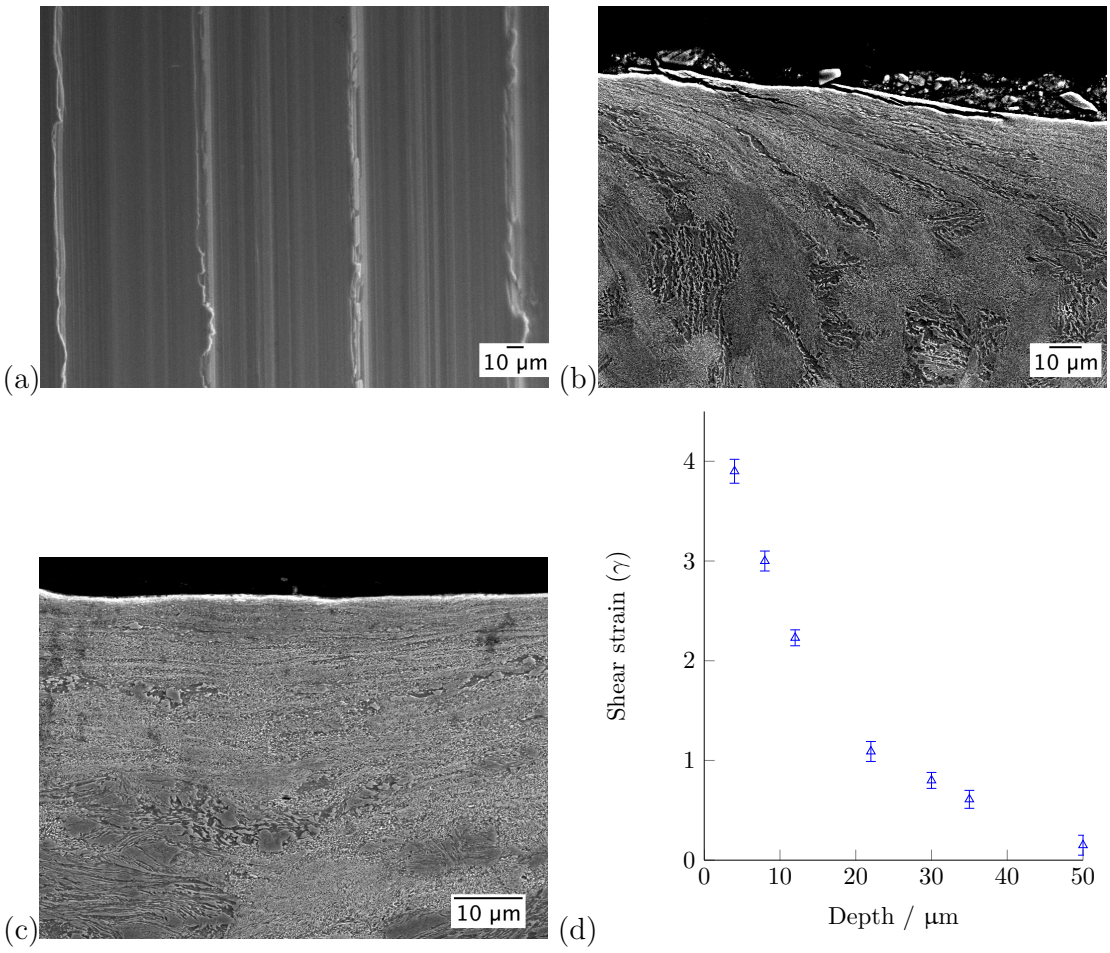

Figure 5: Secondary electron image of the surface and subsurface structure after rolling/sliding (a) Wear tracks on the surface, cross section image (b) along the rolling/sliding direction, (c) along transverse direction and (d) measured shear strain as a function of depth.

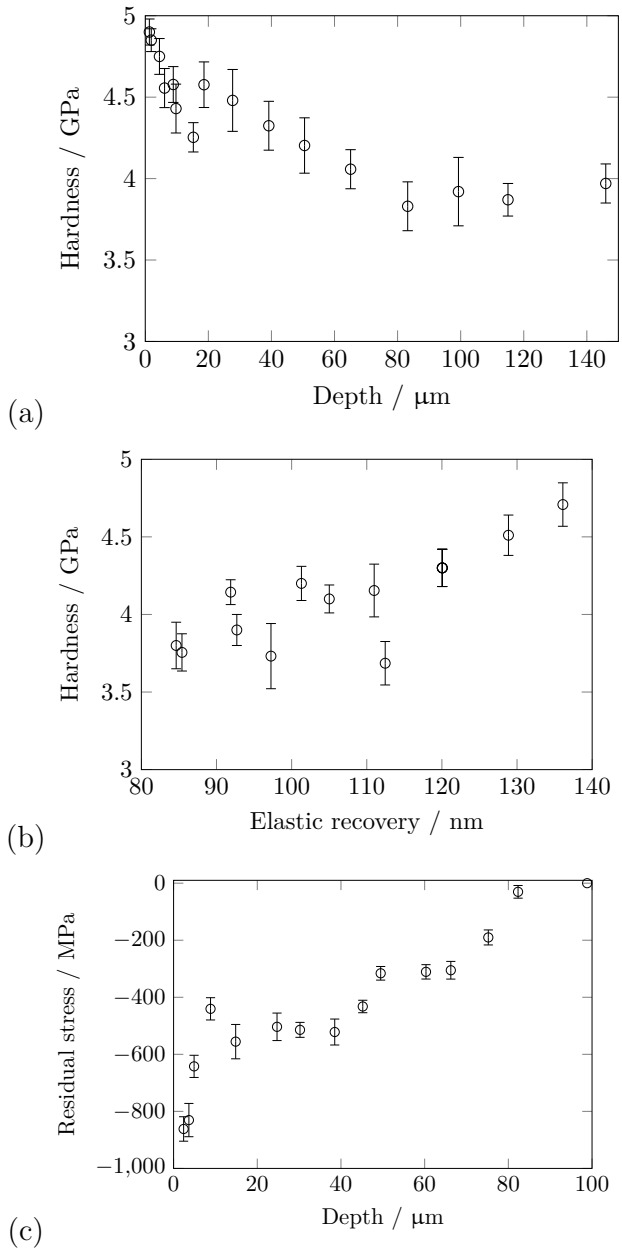

Figure 6: Nanoindentation test results (a) distribution of nanoindentation hardness of the surface and subsurface layers after rolling/sliding, (b) elastic recovery of pearlite after withdrawal of the nanoindentation load and (c) distribution of compressive residual stress along the depth after rolling/sliding.

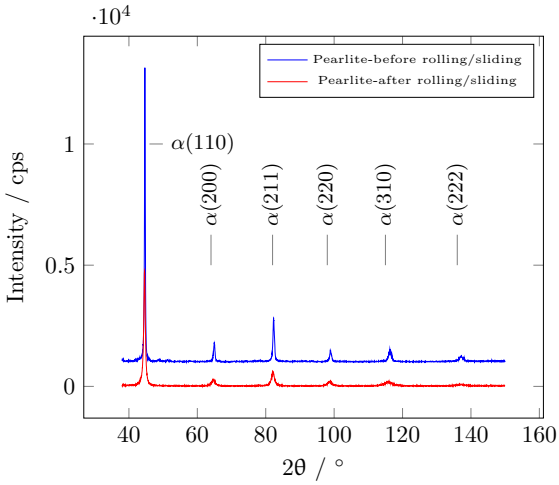

Figure 7: X-ray diffraction profiles from the surface of pearlitic discs before and after rolling/sliding.

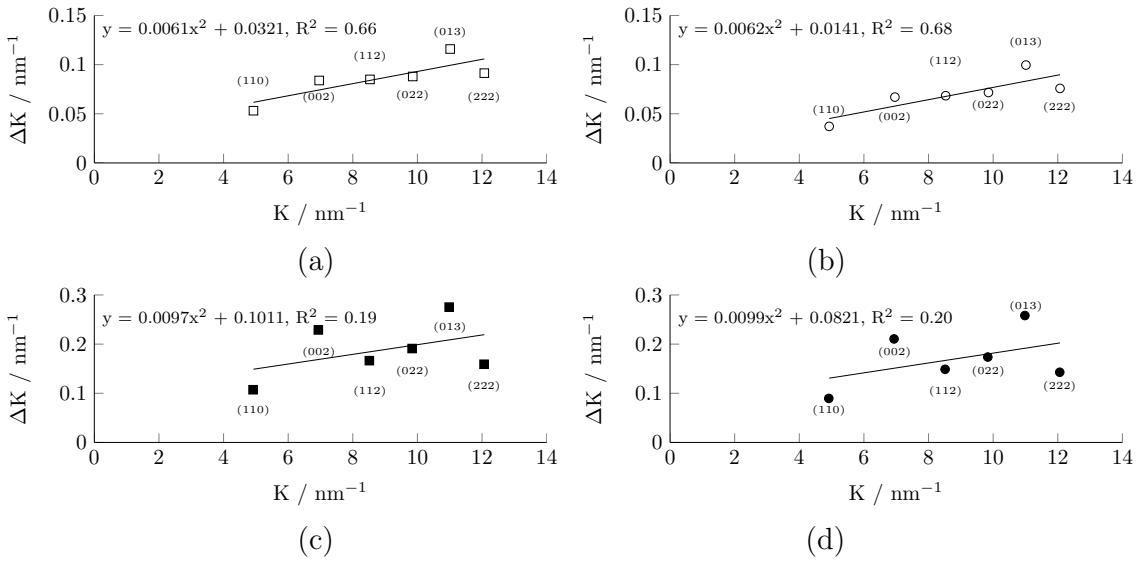

Figure 8: Williamson-Hall plot for ferrite (a) before rolling/sliding assuming Gaussian peak broadening, (b) before rolling/sliding assuming Lorentzian peak broadening, (c) after rolling/sliding assuming Gaussian peak broadening and (d) after rolling/sliding assuming Lorentzian peak broadening.

expressed as;

$$(\Delta K)^2 \cong \left(\frac{k}{D}\right)^2 + \left(\frac{\pi M^2 b^2}{2}\right)\rho K^2 \bar{C}_{hkl} + O(K^4 \bar{C}_{hkl}^2)$$
$$\text{with} \qquad \Delta K = \frac{2\beta\cos\theta}{\lambda}, \quad \mathrm{K} = \frac{2\sin\theta}{\lambda} \tag{2}$$

If the higher order terms of $K\bar{C}^{\frac{1}{2}}$ are neglected then this simplifies to

$$(\Delta K)^2 \cong \left(\frac{k}{D}\right)^2 + \left(\frac{\pi M^2 b^2}{2}\right)\rho K^2 \bar{C}_{hkl} \tag{3}$$

and if $\alpha = (k/D)^2$ and $\beta = \pi M^2 b^2 \rho/2$, eqn.3 becomes

$$[(\Delta K)^2 - \alpha]/K^2 \cong \beta\bar{C} \qquad \begin{cases} \bar{C} = A + BH^2 \\ \alpha = (k/D)^2 \\ \beta = \pi M^2 b^2 \rho/2 \end{cases} \tag{4}$$

where βA and βB are the intercept and slope of the plot of $[(\Delta K)^2 - \alpha]/K^2$ versus H^2. The inverse of βA, written q, helps assess the dislocation character for a particular hkl plane [30, 54, 55]. The value of q was found to change with an initial value prior to deformation of 1.46 to 2.43 after rolling/sliding, indicating the dislocation character of bcc-α changing from edge to screw dislocations [Fig. 10(a)]. The dislocation contrast values were derived from q using the equation

$$\bar{C}_{\{hkl\}} = C_{\{h00\}}(1 - qH^2). \tag{5}$$

To use this equation $\bar{C}_{hkl}$ of $\{200\}$ is first obtained where $H^2 = 0$. Assuming the elastic constants, $c_{11} = 230.1\,\mathrm{GPa}$, $c_{12} = 134.6\,\mathrm{GPa}$ and $c_{44} = 116.6\,\mathrm{GPa}$, $\bar{C}_{200}^{edge}$ for bcc-α Fe has been calculated as 0.2648 and that of $\bar{C}_{200}^{screw}$ is found to be equal to 0.3055 and subsequently $\bar{C}_{hkl}$ for other planes are listed in Table 3 [56].

Table 3: Average dislocation contrast factor of pure edge and pure screw dislocations for hkl planes in bcc-α Fe before rolling/sliding.

	$q = 1.46$		$q = 2.43$	
{hkl}	$\bar{C}_{hkl}^{edge}$	$\bar{C}_{hkl}^{screw}$	$\bar{C}_{hkl}^{edge}$	$\bar{C}_{hkl}^{screw}$
{110}	0.1681	0.1940	0.1040	0.1199
{002}	0.2648	0.3055	0.2648	0.3055
{112}	0.1681	0.1940	0.1040	0.1199
{022}	0.1681	0.1940	0.1040	0.1199
{013}	0.1681	0.1940	0.1040	0.1199
{222}	0.1359	0.1568	0.0503	0.0580

Fig. 8(c-d) can be replotted by introducing the average dislocation contrast factor, $\bar{C}_{\{hkl\}}$ in the term K for pure edge and pure screw dislocations as shown in Fig. 9(a-d) where better correlation to the modified Williamson-Hall function is seen. The average sizes of the coherent domain of diffraction, as calculated using eqn.3 are presented in Table 4 for all combinations of dislocation type and peak shape. The coherent domain sizes are finer than the scale of the starting microstructure, and are reasonable given the finer scale of the deformed state. Since, the actual peak shape is a complex combination of Gaussian and Lorentzian profile, the actual domain size should lie in between 17-23 nm.

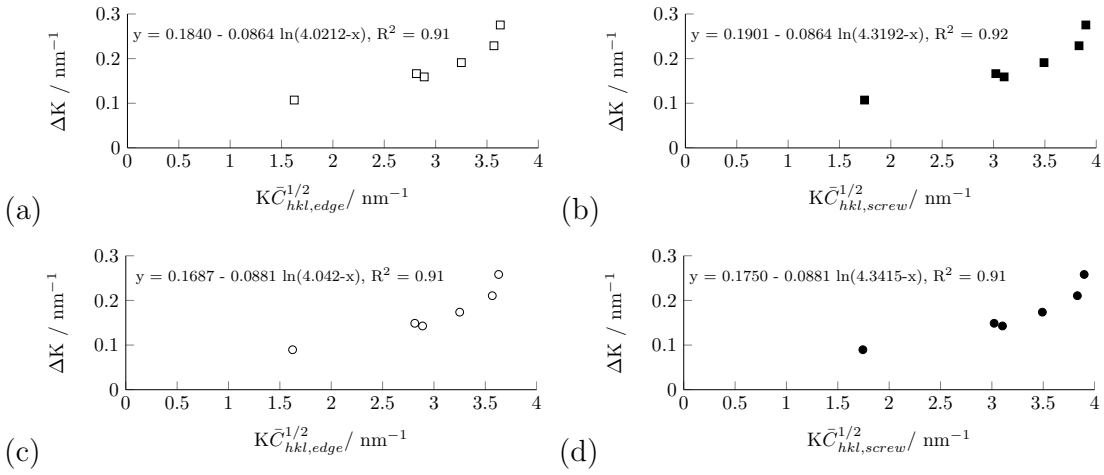

Figure 9: Modified Williamson-Hall plot, according to eqn. 2 for bcc-α considering (a) pure edge dislocation and Gaussian peak broadening, (b) pure screw dislocations and Gaussian peak broadening, (c) pure edge dislocation and Lorentzian peak broadening and (d) pure screw dislocations and Lorentzian peak broadening.

Table 4: Average size of the coherent domains of diffraction in bcc-α of pearlite after rolling/sliding, as a function of the diffraction peak shape.

Dislocation type	Coherent domain size / nm	
	Gaussian	Lorentzian
edge	17	23
screw	17	23

A gradual increase in the dislocation density from 4.0×10^{14} m^{-2} at a depth of 50 μm from the rolling/sliding surface to 7.49×10^{14} m^{-2} near surface has been estimated from the slope of the $(\Delta K)^2$ vs. $K^2\bar{C}_{hkl}$ plot and its variation with depth is shown in Fig. 10(b). Plastic strain at the onset of deformation in ferrite results in rapid multiplication of dislocations. The low mean free path of dislocations in ferrite due to the intervention of cementite lamellae must contribute to the formation dislocation forests with in ferrite. While we do not have quality diffraction data from the cementite, it clearly does undergo plastic deformation, a phenomenon well known in the context of wire drawing [57].

The size of the coherent domain of diffraction can be calculated from the intercept of $(\Delta K)^2$ vs. $K^2\bar{C}_{hkl}$ plot for each depth and the calculated values are plotted against distance from rolling/sliding surface and is shown in Fig. 10(e). It is interesting that the domain size is comparable to that obtained during high pressure torsion tests on pearlite, where the shear strains of the order of 60-200 [58], and indeed, the reported microhardness obtained for this range of shear strain is 4.5-8 GPa. Microhardness probably cannot be related directly to nanohardness, but the range recorded here is from 4-6 GPa, the higher value being below the surface of the sample [Fig. 6(a)]. The lattice parameter of bcc-α as calculated from the X-ray diffraction data obtained from various depths are shown in Fig. 10(c). A marginal increase in the lattice constant for the ferrite has been observed from which the carbon content in ferrite has been calculated following [59],

$$a_\alpha = a_0 + \frac{(a_0 - 0.279x_{\mathrm{C}})^2(a_0 + 2.496x_{\mathrm{C}}) - a_0^3}{3a_0^2} - 0.03x_{\mathrm{Si}} + 0.06x_{\mathrm{Mn}} + 0.07x_{\mathrm{Ni}} + 0.31x_{\mathrm{Mo}} + 0.05x_{\mathrm{Cr}} + 0.096x_{\mathrm{V}} \quad (6)$$

The calculated values of carbon in ferrite is plotted against distance and was found to increase near the surface from that in the bulk [Fig. 10(d)]. It may be possible therefore that some of the cementite which undergoes shear close to the wear surface is induced to dissolve into surrounding ferrite [58]. However, the deduced concentration of carbon in ferrite is not large, and cementite clearly exists at the contact surface, so that the amount of cementite dissolution in the present case is small, consistent with reported atom probe data on wear of pearlite [21]. It should be emphasised that the shear strains involved in the torsion tests are very large, approaching $\gamma = 200$ [58], whereas the maximum measured here is $\gamma \approx 4$, Fig. 5. The fine domain size is therefore not simply a consequence of severe deformation but also due to the very fine starting structure with an interlamellar spacing that is about twice the final domain size.

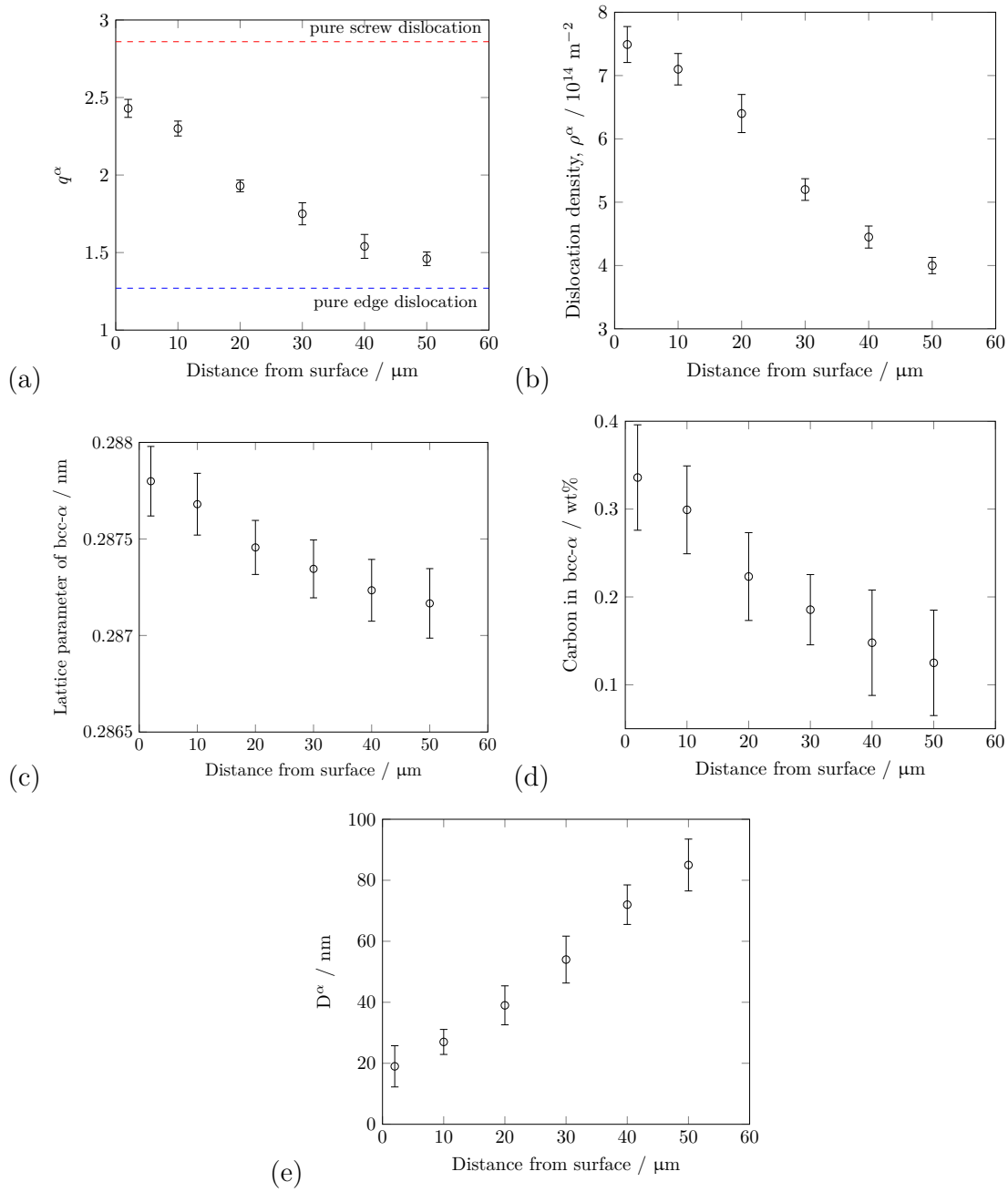

Figure 10: Change in the (a) q parameter, (b) dislocation density, ρ, (c) lattice parameter for ferrite and (d) carbon content in ferrite and (e) coherent domains of diffraction with decreasing distance from core to the rolling/sliding surface.

4. Conclusions

1. It is found that pearlite with a very fine interlamellar spacing can outperform much harder bainitic steels in the context of rolling-sliding wear resistance. The wear causes substantial plastic deformation of the region in the vicinity of the contact surface, with both the ferrite and cementite exhibiting plasticity.
2. The plasticity is not expected from Hertzian analysis that assumes a smooth contact surface. It is likely instead to be a consequence of exaggerated stresses due to surface roughness.
3. The coherent-domain size and hardness resulting from the plastic deformation caused by the wear process is comparable to that encountered in high pressure torsion tests on pearlite. The strains involved in the torsion tests are much larger. Therefore, the fine domain size observed is a consequence of the combined effect of the very small initial interlamellar spacing and the shear strains due to wear. There is evidence based on the lattice parameter of the deformed ferrite, that some of the cementite may have been forced into solution by the plastic strain.
4. The plastic deformation of the surface during the rolling-sliding test has been shown to introduce compressive stresses into the surface. This must help reduce the wear rate. The residual stress described here is conventionally known as Type II, i.e., on the scale of a few grains.

Acknowledgements: SDB thanks Tata Steel Limited, India for generously funding this project.

References

1. D. M. Fegredo, and C. Pritchard: 'A metallographic examination of rollers subjected to wear under rolling-sliding conditions', *Wear*, 1978, **49**, 67 – 78.

2. T. Yamada: 'Rolling wear characteristics of annealed carbon steels under dry contact conditions', *Wear*, 1978, **51**, 279 – 288.

3. P. Clayton, and D. Danks: 'Effect of interlamellar spacing on the wear resistatnce of eutectoid steels under rolling–sliding conditions', *Wear*, 1990, **135**, 369–389.

4. J. E. Garnham, and J. H. Beynon: 'Dry rolling-sliding wear of bainitic and pearlitic steels', *Wear*, 1992, **157**, 81–109.

5. A. Ramalho, M. Esteves, and P. Marta: 'Friction and wear behaviour of rolling–sliding steel contacts', *Wear*, 2013, **302**, 1468–1480.

6. T. M. Beagley: 'Severe wear of rolling/sliding contacts', *Wear*, 1976, **36**(3), 317 – 335.

7. D. Danks, and P. Clayton: 'Comparison of the wear process for eutectoid rail steels: Field and laboratory tests', *Wear*, 1987, **120**, 233 – 250.

8. M. Sato, P. M. Anderson, and D. A. Rigney: 'Rolling-sliding behaviour of rail steels', *Wear*, 1993, **162-164**, 159–172.

9. P. Clayton: 'The relations between wear behaviour and basic material properties for pearlitic steels', *Wear*, 1980, **60**, 75–93.

10. P. Clayton, and R. Devanathan: 'Rolling/sliding wear behavior of a chromium-molybdenum rail steel in pearlitic and bainitic conditions', *Wear*, 1992, **156**, 121 – 131.

11. F. Katsuki, and M. Yonemura: 'Subsurface characteristics of an abraded Fe-0.4 wt%C pearlitic steel: A nanoindentation study', *Wear*, 2007, **263**, 1575–1578.

12. A. J. Perez-Unzueta, and J. H. Beynon: 'Microstructure and wear resistance of pearlitic rail steels', *Wear*, 1993, **162-163**, 173–182.

13. F. T. Barwell: 'The effect of lubrication and nature of superficial layer after prolonged periods of running', In: *Symposium on Properties of Metallic Surfaces, Institute of Metals Monograph and Report No. 13*. London, U.K.: Insitute of Metals, 1953:101–122.

14. F. Barwell: 'Wear of metals', *Wear*, 1958, **1**, 317 – 332.

15. D. M. Fegredo, J. Kalousek, and M. T. Shehata: 'The effect of progressive minor spheroidization on the dry-wear rates of a standard carbon and a Cr-Mo alloy rail steel', *Wear*, 1993, **161**, 29 – 40.

16. T. Takahashi, and M. Nagumo: 'Flow stress and work-hardening of pearlitic steel', *Trans. JIM*, 1970, **11**, 113–119.

17. J. D. Grozier, and J. H. Bucher: 'Correlation of fatigue limit with microstructure and composition of ferrite-pearlite steels', *Journal of Matererials*, 1967, **2**, 393 – 407.

18. G. M. da Fonseca Gomes, L. H. de Almeida, L. C. F. Gomes, and I. L. May: 'Effects of microstructural parameters on the mechanical properties of eutectoid rail steels', *Materials Characterization*, 1997, **39**, 1 – 14.

19. J.Larsen-Badse, and K.G.Mathew: 'Influence of structure on the abrasion resistance of a 1040 steel', *Wear*, 1969, **14**, 199–206.

20. D. A. Rigney: 'Viewpoint set on materials aspects of wear-introdection', *Scripta Materialia*, 1990, **24**, 799 – 803.

21. J. Takahashi, Y. Kobayashi, M. Ueda, T. Miyazaki, and K. Kawakami: 'Nanoscale characterisation of rolling contact wear surface of pearlitic steel', *Materials Science and Technology*, 2013, **29**, 1212–1218.

22. K. M. Wu, and H. K. D. H. Bhadeshia: 'Extremely fine pearlite by continuous cooling transformation', *Scripta Materialia*, 2012, **67**, 53–56.

23. H. K. D. H. Bhadeshia: 'The first bulk nanostructured metal', *Science and Technology of Advanced Materials*, 2013, **14**, 014202.

24. W. C. Oliver, and G. M. Pharr: 'Measurement of hardness and elastic modulus by instrumented indentation: Advances in understanding and refinements to methodology', *Journal of Materials Research*, 2004, **19**, 3–20.

25. J. Woirgard, and J.-C. Dargenton: 'An alternative method for penetration depth determination in nanoindentation measurements', *Journal of Materials Research*, 1997, **12**(9), 2455–2458.

26. Y. Bao, L. Liu, and Y. Zhou: 'Assessing the elastic parameters and energy-dissipation capacity of solid materials: A residual indent may tell all', *Acta Materialia*, 2005, **53**, 4857 – 4862.

27. Q. Wang, K. Ozaki, H. Ishikawa, S. Nakano, and H. Ogiso: 'Indentation method to measure the residual stress induced by ion implantation', *Nuclear Instruments and Methods in Physics Research Section B: Beam Interactions with Materials and Atoms*, 2006, **242**, 88 – 92.

28. M. Sakai, and Y. Nakano: 'Elastoplastic load–depth hysteresis in pyramidal indentation', *Journal of Materials Research*, 2002, **17**, 2161–2173.

29. T. Ungar: 'Dislocation densities, arrangements and character from X-ray diffraction experiments', *Materials Science and Engineering A*, 2001, **309–310**, 14 – 22.

30. E. Schafler, M. Zehetbauer, and T. Ungar: 'Measurement of screw and edge dislocation density by means of X-ray Bragg profile analysis', *Materials Science and Engineering A*, 2001, **319-321**, 220–223.

31. J. E. Garnham, and C. L. Davis: 'The role of deformed rail microstructure on rolling contact fatigue initiation', *Wear*, 2008, **265**, 1363 – 1372.

32. E. E. Underwood: Quantitative Stereology: Addison–Wesley Publication Company, 1970.

33. K. K. Ray, and D. Mondal: 'Effect of interlamellar spacing on strength of pearlite in annealed eutectoid and hypoeutectoid plain carbon steels', *Acta Metallurgica and Materialia*, 1991, **39**, 2201–2208.

34. B. E. Q'Donnelly, R. L. Reuben, and T. N. Baker: 'Quantitative assessment of strengthening parameters in ferrite-pearlite steels from microstructural measurements', *Metals Technology*, 1984, **11**, 45–51.

35. E. M. Taleff, J. J. Lewandowski, and B. Pouladian: 'Microstructure-property relationships in pearlitic eutectoid and hypereutectoid carbon steels', *Journal of Metals*, 2002, **54**, 25–30.

36. S. D. Bakshi, P. H. Shipway, and H. K. D. H. Bhadeshia: 'Three-body abrasive wear of fine pearlite, nanostructured bainite and martensite', *Wear*, 2013, **308**, 46–53.

37. A. Kapoor, F. J. Franklin, S. K. Wong, and M. Ishida: 'Surface roughness and plastic flow in rail wheel contact', *Wear*, 2002, **253**, 257–264.

38. S. D. Bakshi, A. Leiro, B. Prakash, and H. K. D. H. Bhadeshia: 'Dry rolling/sliding wear of nanostructured bainite', *Wear*, 2014, **316**, 70–78.

39. T. Sourmail, F. G. Caballero, C. Garcia-Mateo, V. Smanio, C. Ziegler, M. Kuntz, R. Elvira, A. Leiro, E. Vuorinen, and T. Teeri: 'Evaluation of potential of high Si high C steel nanostructured bainite for wear and fatigue applications', *Materials Science and Technology*, 2013, **29**, 1166–1173.

40. A. Basak, D. C. Reddy, and D. V. K. Kanth: 'Computer modelling of wear resistance for plain carbon steels', *Materials Science and Technology*, 1998, **14**, 776–782.

41. K. L. Johnson: Contact Mechanics: Cambridge, U. K.: Cambridge University Press, 1985.

42. L. WenTao, Y. Zhang, F. ZhiJing, and Z. JingShan: 'Effects of stick-slip on stress intensity factors for subsurface short cracks in rolling contact', *Science China Technological Sciences*, 2013, **56**, 2413–2421.

43. H. C. Eden, J. E. Garnham, and C. L. Davis: 'Influential microstructural changes on rolling contact fatigue crack initiation in pearlitic rail steels', *Materials Science and Technology*, 2005, **21**, 623–629.

44. J. Gil-Sevillano: 'Room temperature plastic deformation of pearlitic cementite', *Materials Science & Engineering*, 1975, **21**, 221–225.

45. G. Langford: 'Deformation of pearlite', *Metall. Trans. A*, 1977, **8**, 861 – 875.

46. J. Kalousek, D. M. Fegredo, and E. E. Laufer: 'The wear resistance and worn metallography of pearlite, bainite and tempered martensite rail steel microstructure of high hardness', In: K. C. Ludema, ed. *Proceedings of the 6th International Conference on Wear of Material,*. New York, USA: American Society of Mechanical Engineers, 1987:212–231.

47. W. R. Tyfour, J. H. Beynon, and A. Kapoor: 'The steady state wear behaviour of pearlitic rail steel under dry rolling-sliding contact conditions', *Wear*, 1995, **180**, 79 – 89.

48. J. H. Beynon, J. E. Garnham, and K. J. Sawley: 'Rolling contact fatigue of three pearlitic rail steels', *Wear*, 1996, **192**, 94 – 111.

49. S. Jahanmir, and N. P. Suh: 'Mechanics of subsurface void nucleation in delamination wear', *Wear*, 1977, **44**, 17 – 38.

50. J. W. Ho, C. Noyan, and J. B. Cohen: 'Residual stress and sliding wear', *Wear*, 1983, **84**, 183–202.

51. P. J. Withers, and H. K. D. H. Bhadeshia: 'Residual stress part 2 - nature and origins', *Materials Science and Technology*, 2001, **17**, 366–375.

52. T. Ungar, I. Dragmoir, A. Revesz, and A. Borbely: 'The contrast factors of dislocations in cubic crystals: the dislocation model of strain anisotropy in practice', *Journal of Applied Crystallography*, 1999, **32**, 992.

53. T. Ungar, S. Ott, P. G. Sanders, A. Brobely, and J. R. Weertman: 'Dislocations, grain size and planar faults in nanostructured copper determined by high resolution x-ray diffraction and a new procedure of peak profile analysis', *Acta Materialia*, 1998, **46**, 3693–3699.

54. T. Ungar: 'Dislocation densities, arrangements and character from X-ray diffraction experiments', *Materials Science & Engineering, A*, 2001, **309–310**, 14–22.

55. T. Shintani, and Y. Murata: 'Evaluation of the dislocation density and dislocation character in cold rolled type 304 steel determined by profile analysis of X-ray diffraction', *Acta Materialia*, 2011, **59**, 4314–4322.

56. N. Armstrong, and P. Lynch: Determination of the dislocation contrast factor for X-ray line profile analysis in : Diffraction Analysis of the Microstructure of Materials, vol. 68: Germany: Springer, eds E. J. Mittemeijer and P. Scardi, 2004.

57. X. D. Zhang, A. Godfrey, W. Liu, and Q. Liu: 'Study on dislocation slips in ferrite and deformation of cementite in cold drawn pearlitic steel wires from medium to high strain', *Materials Science and Technology*, 2011, **27**, 562–567.

58. Y. Ivanisenko, W. Lojkowski, R. Z. Valiev, and H. J. Fecht: 'The mechanism of formation of nanostructure and dissolution of cementite in a pearlitic steel during high pressure torsion', *Acta Materialia*, 2003, **51**, 5555–5570.

59. D. J. Dyson, and B. Holmes: 'Effect of alloying additions on the lattice parameter austenite', *Journal of the Iron and Steel Institute*, 1970, **208**, 469–474.